Josephson and noise scanning tunneling microscopy on conventional, unconventional and disordered superconductors

Chatzopoulos, D.

2

Introduction to Josephson and noise scanning tunneling microscopy

Throughout the research work presented in this thesis, Josephson and noise scanning tunneling microscopy are employed as means to probe the superfluid and the charge of conventional, iron-based and disordered superconductors. This chapter is dedicated to analysing those techniques in more detail. We start by quickly reviewing the basic principles of scanning tunneling microscopy. Afterwards we describe the working principles and challenges of Josephson and noise spectroscopy while focusing on some theory aspects as well.

Parts of this chapter have been published in *Nature* **571**, 541-545 (2019), Physical Review B **100**, 104506 (2019) and *Rev. Sci. Instrum.* **89**, 093709 (2018).

2.1. Scanning tunneling microscopy

Scanning tunneling microscopy (STM) was invented in 1982 by Binnig and Rohrer [1] (Nobel prize in 1986). STM is a unique technique not only for imaging and manipulating individual atoms but also for performing spectroscopy with atomic resolution. It uses a sharp metallic tip on an electrically conducting sample surface under voltage bias (V_{bias}), in order to record the tunneling current I_{T} of electrons between the two (see Fig. 2.1a). By raster scanning the tip on the surface with sub-Å resolution (using piezoelectric scanners) one is able to record the tunneling current as a function of space (x, y) and voltage bias. It can be shown that the tunneling current I_{T} depends exponentially on the distance between tip and sample Δz

$$I_{\text{T}} \propto \exp(-\kappa \Delta z), \tag{2.1}$$

where κ is a constant related to the tunneling barrier between tip and sample. This makes the STM extremely sensitive to surface modulations on the atomic scale. In more detail, atomically resolved topographic information of the surface can be obtained using a feedback loop that maintains I_{T} constant by adjusting the tip height (using again a piezoelectric scanner), while the tip is rastered over the sample surface (voltage bias is fixed during scanning).

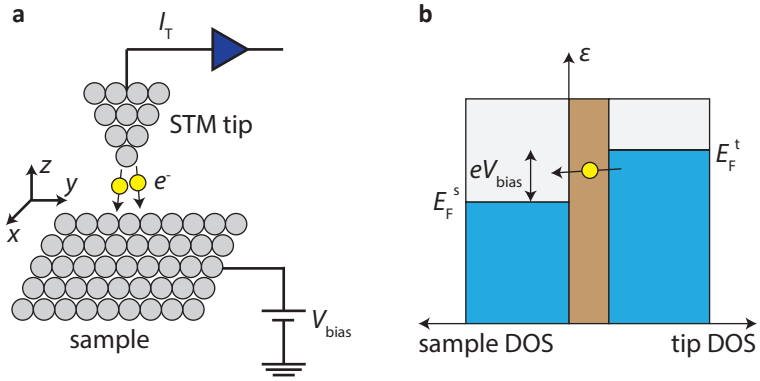

Figure 2.1: **STM schematics. a** Schematic of an STM jucntion. Gray circles denote atoms. An atomically sharp metallic tip is in tunneling distance to the flat surface of a voltage-biased sample. Electrons (yellow circles) tunnel through the vacuum barrier separating the tip and sample. The tunneling current I_{T} is first amplified (blue triangle) and subsequently measured (not shown). **b** Simplified density of states (DOS) diagram for an STM junction. The filled (empty) states in the DOS of the tip (t) and the sample (s) are denoted with blue (gray) areas. The difference in the Fermi energies equals the bias voltage eV_{bias}. An electron tunnels from filled states on the tip through the vacuum barrier (brown-shaded area) to occupy empty states on the sample at lower energy.

It is worthwhile mentioning that in order to get a stable STM junction and achieve atomic resolution imaging, an atomically sharp tip and flat sample surface are needed. Therefore, scanning tunneling microscopists usually employ special tip treatment and sample cleaning recipes at (ultra) high vacuum that allow them to perform high quality STM. In addition, since I_{T} typically ranges from tens of picoamperes (pA) to a few nanoamperes (nA), it is equally important to perform STM

measurements in ultra low mechanical and acoustic vibration conditions such that unwanted noise is minimized.

Apart from gaining insight to the surface information of a material, via STM one is also able to perform tunneling spectroscopy. This is achieved by recording the tunneling current as a function of voltage bias. Typically, the tip is parked at the location of interest and the tunneling current is measured while the voltage bias is sweeped with the feedback loop turned off. To avoid unwanted signal noise in the measurement it is very typical that lock-in amplifier techniques are employed for recording the tunneling conductance of the junction as a function of voltage bias. The latter turns out to provide information about the density of states (DOS) of the sample. A schematic of the tunneling process taking place in an STM involving the DOS of the tip and the sample is shown in Fig. 2.1b. The tunneling conductance dI/dV, using Fermi's Golden rule under some reasonable approximations and at sufficiently low temperatures, reads [2]

$$\frac{dI}{dV} = -\frac{4\pi e^2}{\hbar} \exp\left(-\kappa \Delta z\right) \rho_{\mathrm{t}}(0) \rho_{\mathrm{s}}(eV). \tag{2.2}$$

Here, $\rho_{\mathrm{t(s)}}(eV)$ is the DOS of the tip (sample) calculated at energy equal to eV ($V = V_{\mathrm{bias}}$). From the expression above we see that STM conductance spectroscopy directly probes the DOS of the sample. Thus, combining dI/dV spectroscopy with the scanning capabilities of STM, one retrieves spatially resolved information about the sample DOS variations with atomic resolution.

Thus, STM is a very powerful tool to investigate nanoscale electronic inhomogeneities in contrast to bulk probe techniques.

Apart from real space information on the electronic properties of a material, the *quasiparticle interference* technique (QPI) using an STM provides insight to the momentum space. QPI is based on the interference of quasiparticle waves in a material. In metals, electrons are described as Bloch waves (characterised by wavevectors k) yielding a local DOS (LDOS) that reads

$$\mathrm{LDOS}(\epsilon, \mathbf{r}) \propto \sum_{\mathrm{k}} |\psi_{\mathrm{k}}(\mathbf{r})|^2 \delta(\epsilon - E_{\mathrm{k}}), \tag{2.3}$$

where $\psi_{\mathrm{k}}(\mathbf{r})$ are the eigenstates in k-space and E_{k} the dispersion relation in the metal ($\delta(\epsilon)$ is the delta function). In contrast to angle-resolved photoemission spectrocopy (ARPES), STM cannot retrieve direct information about the dispersion E_{k}. However, Bloch-waves can scatter off crystal imperfections, impurity atoms, vortices etc. Such scattering processes are elastic and cause mixing of eigenstates with different k having the same dispersion. The mixing of two Bloch waves (say k_1 and k_2), results into standing waves described by a wavefunction ψ_{q}, with $\mathrm{q} = (\mathrm{k}_1 - \mathrm{k}_2)/2$. Such standing waves are detectable in an STM experiment, since the LDOS is proportional to the dI/dV signal as we showed before. Thus the dI/dV signal in real space at fixed energy exhibits spatial oscillations, usually around scattering centres, with a wavelength equal to π/q. Typically one takes the Fourier

transform of the real space images and identify the dominant scattering wavevectors q. In general, a challenge in the QPI method is to identify the wavevectors that contributed to the standing wave q without any prior information about the actual band structure of the material at hand. For this reason, a combination of ARPES and STM experiments is required in order to capture the complete picture.

Concerning STM on superconducting surfaces that are the main focus of this thesis, it was not until the end of the 80s that the first cryogenic STM was employed for the first time on a superconductor. In one of the first experiments at 4.2 K, the superconducting gaps of Pb, PbBi and NbN were measured by employing a metallic gold tip [3], to find good agreement with the predictions of BCS theory. In addition several other works investigated the variations of the superconducting state (energy gap) in space using low temperature STM [4, 5]. Later on, the vortices in a superconductor ($NbSe_2$) were imaged by Hess et al [6, 7] for the first time, and their electronic structure was investigated in terms of spectroscopy. Over the years, there have been several important experiments employing STM tips on conventional superconductors. Experimental works on, magnetic adsorbates on superconductors [8, 9], the superconducting proximity effect [10, 11], the double-gap structure of Pb [12] and the confinement of quasiparticles in Pb (111) quantum wells [13], are only a handful of examples.

Experimental works using STMs on unconventional superconductors have proven to be equally valuable in understanding these correlated electron materials that cannot be described by BCS theory. In fact, STM is probably the most suitable tool for revealing the nanoscale electronic inhomogeneities in unconventional superconductors given its unique combination of imaging and spectroscopic capabilities. A vast amount of experimental work has been focussing on cuprate materials and in particular in identifying their pairing symmetry, addressing their gap inhomogeneities etc [14]. In addition the QPI method has been used with great success as a sign-sensitive probe of the order parameter [15]. As one might expect, the STM probing techniques have also made significant contribution on providing insight on other classes of unconventional superconductors such as the iron-based family [2] and the heavy fermion compounds [16].

2.2. Josephson scanning tunneling microscopy

Josephson scanning tunneling microscopy (JSTM) [17] is a technique that involves tunneling microscopy using a superconducting tip with the ultimate goal to probe the superfluid density of the material at hand. In conventional STM methods a metalic tip is used in order to probe the electronic and topographic properties of the material via tunneling of single-particle carriers between the tip and the sample. In strike contrast, in the JSTM method the use of a superconducting tip and sample opens a new tunneling window for Cooper pairs in addition to the conventional one for quasi-particles. Importantly, STM imaging with unprecedented resolution combined with the Josephson tunneling method allows one to map the superconducting order parameter in the atomic scale.

As the name of the technique suggests, JSTM is based on the phenomenon of Cooper pair tunneling described by Brian Josephson in his celebrated work in

1962 [18]. In JSTM, a junction is formed between an STM tip and a sample (both superconducting) that are separated by a vacuum barrier (Fig. 2.2).

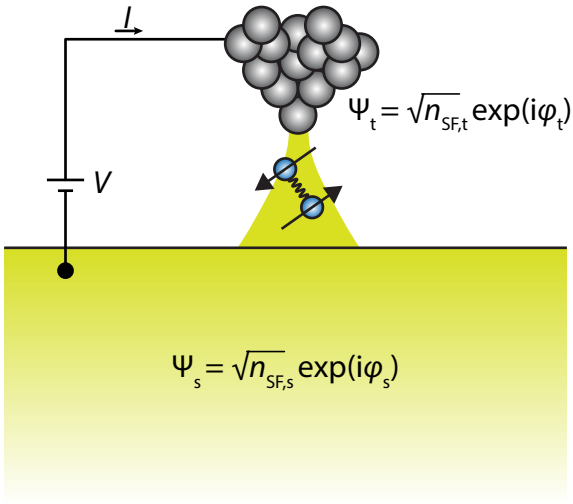

Figure 2.2: **Schematic representation of a Josephson junction in STM.** A STM tip (gray circles) is in tunneling distance with the sample (yellow shaded region). Both are superconducting and their macroscopic wavefunction can be written as $\Psi_{s(t)} = \sqrt{n_{SF,s(t)}}\exp(i\phi_{s(t)})$. In such a Josephson junction a Cooper pair (blue circles) tunnels through the vacuum barrier between tip and sample.

It is instructive to show that the tunneling current of Cooper pairs predicted by Josephson contains information about the order parameter of the superfluid in both the sample and the tip. We start by writing an expression for the macroscopic wavefunction ($\Psi_{s(t)}$) of the superconducting condensate in the tip (t) and the sample (s). These read

$$\Psi_{s(t)} = \sqrt{n_{SF,s(t)}}\exp(i\phi_{s(t)}). \tag{2.4}$$

Here $|\Psi_{s(t)}|^2 = n_{SF,s(t)}$ is the superfluid density which corresponds to the order parameter and $\phi_{s(t)}$ is the phase of the condensate in the sample or tip. Assuming a junction that is one dimensional, the probability current is given by

$$j = \frac{\hbar}{4im}\left(\Psi_J^* \frac{d\Psi_J}{dx} - \Psi_J \frac{d\Psi_J^*}{dx}\right), \tag{2.5}$$

and represents the supercurrent resulting from Cooper pair tunneling. In the formula above $\hbar$ is Planck's constant, i is the imaginary unit and m the electron mass (note the factor 4 in the denominator that accounts for the fact that Cooper pairs have a mass of $2m$). Moreover, we denote complex conjucation by using the $*$ symbol. Our next step is to approximate the total wavefunction Ψ_J of the junction

and its derivative $d\Psi_J/dx$. Substituting

$$\begin{aligned} \Psi_J &= \frac{\Psi_s + \Psi_t}{2} \\ \frac{d\Psi_J}{dx} &= \Psi_s - \Psi_t, \end{aligned} \tag{2.6}$$

in 2.5 we find that the supercurrent follows the Josephson relation

$$I_S = I_C \sin(\phi_s - \phi_t), \tag{2.7}$$

with

$$I_C = \frac{\hbar}{2m}\sqrt{n_{SF,s}}\sqrt{n_{SF,t}}, \tag{2.8}$$

being the maximum (critical) supercurrent that the junction can sustain. Hence, assuming the superfluid density in the tip to be constant, one can treat the critical supercurrent as a measure for probing the superfluid density (order parameter) in the sample.

At this point it important to note that the procedure we followed above is rather simple. The Josephson relation in 2.7 can be shown using microscopic descriptions that are far more complete. In addition, Josephson junctions based on the Josephson effect have been studied extensively in mesoscopic systems and have been exploited in numerous applications including superconducting quantum interference devices [19] and quantum bits [20].

Now that we have shown that the supercurrent carries information about the superfluid density, our next task is to identify its current and conductance signatures in a STM experiment. In a JSTM experiment we sweep the applied bias V between tip and sample and we record the current I and conductance dI/dV of the junction. In order to identify the supercurrent signatures we will take a closer look in the available models that predict the $I-V$ characteristics of a Josephson junction. Since each model has specific assumptions and limitations we will first analyse the relevant energy scales involved in JSTM. These will help us to identify the applicability of each model.

2.2.1. Energy scales in Josephson STM

We start with a description of the measurement circuit in a typical JSTM experiment as shown in Fig. 2.3. The corresponding circuit diagram of this Josephson junction involves the following key components:

- the critical supercurrent I_C;
- the junction resistance R_J;
- the junction capacitance C_J, biased by a voltage source at V;
- the complex impedance $Z(\omega)$, which corresponds to the electromagnetic environment of the junction and accounts for any form of dissipation that may be present.

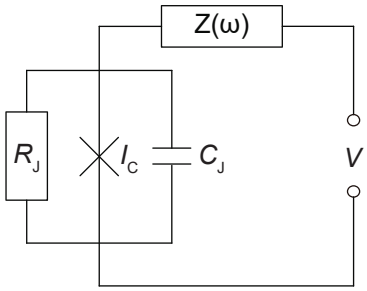

Figure 2.3: **Circuit diagram of a Josephson junction in STM.** The Josephson junction with maximum critical supercurrent I_C is biased with a voltage V. The junction has a resistance R_J and capacitance C_J. To account for dissipation effects a complex impedance $Z(\omega)$ is connected in series with the junction.

The relevant energy scales in such ultra-small junctions are:

- The **charging energy** $E_C = (2e)^2/(2C_J)$ which is related to the Coulomb energy change that occurs when a Cooper pair tunnels across an ultra-small junction. Note that Cooper pairs carry charge of $2e$ in the formula above.
- The **Josephson energy** $E_J = \hbar I_C/(2e)$ being a measure of how strongly the two superconducting condensates forming the junction are coupled to each other (for this reason, it is also called coupling energy [21]) and is proportional to the critical supercurrent.
- The **thermal energy** (also known as thermal noise) $E_T = k_B T$ corresponds to the kinetic energy due to non-zero temperature (k_B is the Boltzmann constant).

In contrast to planar mesoscopic junctions, ultra-small JSTM junctions have larger Coulomb energy E_C. We estimate $C_J \approx 1$ fF for an STM junction and thus $E_C = 276$ μeV (about 3.2 K). In addition, a typical tunnelling junction has a relatively large junction resistance R_J (>0.1 MΩ). Using the formula suggested by Ambegaokar and Baratoff [22]

$$E_J = \frac{\pi\hbar}{4e^2}\frac{\Delta}{R_J}\tanh\left(\frac{\Delta}{2k_B T}\right) \tag{2.9}$$

the Josephson energy E_J corresponds to 3.5 μeV (about 40 mK) for a symmetric Josephson junction with junction resistance $R_J = 1$ MΩ and pair-breaking gap $\Delta = 1$ meV. It is important to compare these relevant energy scales to be able to choose the applicable model to describe the current–voltage (I–V) characteristics of the junction, and to eventually extract the superconducting order parameter, as we emphasized previously. In the experiments that we conducted in Chapter 3, E_J is smaller than both the measurement temperature (2.2 K) and E_C ($E_C \geq E_J$).

At this point we are ready to discuss the different frameworks that have been developed in order to describe the I–V characteristics of a Josephson junction.

The three most commonly used ones are the resistively and capacitive shunted Josephson junction (RCSJ) model, the IZ model and $P(E)$ theory.

2.2.2. The RCSJ model

The standard RCSJ model [23, 24] is applicable when the junction is isolated from its electromagnetic environment ($Z(\omega) = 0$), and temperature fluctuations are usually neglected ($E_T < E_J$). In this model one solves the equation describing the temporal evolution of the phase difference $\Delta\phi = \phi_s - \phi_t$ for each current–bias (I_B) condition. This reads

$$C_J\dot{V} + \frac{1}{R_J}V + I_C \sin(\Delta\phi) = I_B. \tag{2.10}$$

The voltage drop across the junction is then calculated from the time derivative of the phase difference according to the Josephson relation [21]

$$V = \frac{\hbar}{2e}\frac{d\Delta\phi}{dt}. \tag{2.11}$$

The evolution of the phase is similar to that of a classical particle moving in a tilted-washboard potential landscape,

$$U = E_J\left[1 - \cos(\Delta\phi) - \frac{I_B}{I_C}\Delta\phi\right]. \tag{2.12}$$

This is illustrated in Fig. 2.4a. When the bias current is $I_B \leq I_C$, the particle is trapped inside a potential minimum, resulting in zero voltage drop across the junction because $d(\Delta\phi)/dt = 0$. For $I_B \geq I_C$, the potential minima are not deep enough to trap the particle. In this case, the phase evolves in time, and a voltage drop proportional to I_B is observed.

The $I{-}V$ characteristics are affected significantly by the so called Stuart-McCumber parameter [23, 24]

$$\beta_C = \frac{2\pi}{\Phi_0}I_C R_J^2 C_J, \tag{2.13}$$

where Φ_0 is the magnetic flux quantum. As shown in Fig. 2.4b, a typical I–V curve calculated using the RCSJ model for $\beta_c = 0$ (i.e. $C_J = 0$) clearly exhibits a current equal to I_C at zero bias. In this regime ($\beta_c \ll 1$) the junction is strongly over-damped and is the most common approximation used in practice. In the strongly underdamped limit ($\beta_c \gg 1$) the $I - V$ characteristics are highly hysteretic when a full current bias sweep is performed (for a more detailed description see [21]).

2.2.3. The IZ model

When temperature fluctuations become important ($E_T > E_J$: see Fig. 2.5a) and for the simplest case of an Ohmic environment $Z(\omega) = Z = R$, the RCSJ model can be solved analytically. In this phase-diffusive limit, Ivanchenko and Zil'berman calculated the I–V characteristics [25] to find that the effect of the environment is introduced by a finite slope at zero bias

$$I_{IZ}(V) = \frac{I_C^2 Z}{2}\frac{V}{V^2 + V_C^2}, \tag{2.14}$$

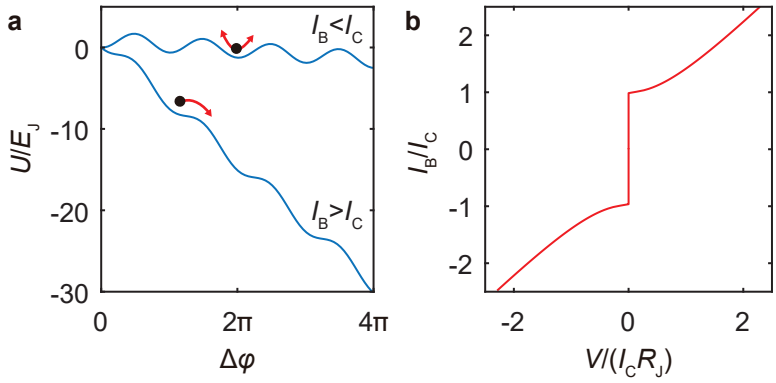

Figure 2.4: **The RCSJ model. a** The tilted washboard potential for different bias conditions (I_B/I_C = 0.1, 1.2) as calculated from equation 2.12. **b** $I-V$ characteristics calculated using the RCSJ model for $\beta_c = 0$.

where $V_C = 2eZk_BT/\hbar$. In this case the critical supercurrent I_C can be extracted from the maximum in the I–V characteristics or from the zero-bias peak height in the dI/dV spectrum, as shown in Fig. 2.5.

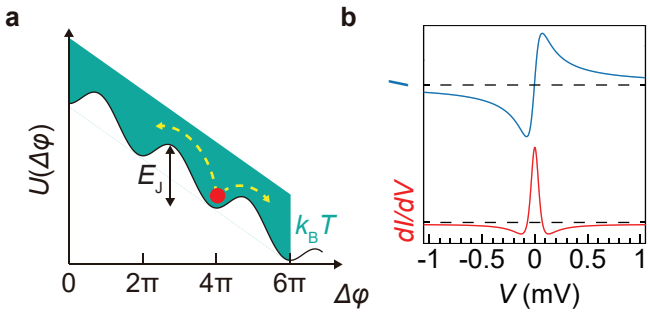

Figure 2.5: **The IZ model. a** Thermal phase fluctuations (illustrated by yellow dashed arrows) in the tilted-washboard potential. **b** I–V and corresponding differential conductance dI/dV, calculated using the IZ model for $Z(\omega) = R$ and the phase-diffusive regime ($E_T > E_J$). For the simulation we used $R = 1$ kΩ and $T = 2$ K.

In more detail, according to the IZ model, the maximum ($I_{\max}$) in the I–V characteristic curves is related to the critical supercurrent according to the formula

$$I_{\mathrm{C}} = \sqrt{\frac{8 I_{\max} e k_{\mathrm{B}} T}{\hbar}}. \tag{2.15}$$

Hence, we can extract the maximum from a measured I–V curve around zero bias and use the above formula for quantifying I_{C}. Alternatively, one may fit the measured spectra with equation 2.14 and extract the critical supercurrent. As we will see in Chapter 3, the latter method was employed.

2.2.4. $P(E)$ theory

When an arbitrary dissipative environment $Z(\omega)$ is present and $E_{\mathrm{C}} > E_{\mathrm{J}}$, a quantum mechanical treatment of the phase fluctuations is necessary. In this regime, $P(E)$ theory is the most suitable [26, 27]. The formalism is based on the $P(E)$ function, which is central in this framework in order to calculate the $I - V$ characteristics of the junction. In $P(E)$ theory one starts with a simple Hamiltonian

$$H = H_{\mathrm{env}} + E_{\mathrm{J}} \cos(2\Delta\phi) \tag{2.16}$$

where the first term takes into account the effects of the interaction of the Josephson junction with the electromagnetic environment. The second term is a tunneling Hamiltonian term for Cooper pairs. The environment is typically modelled as a collection of infinite Bosonic modes, firstly introduced by Caldera and Leggett [28]. Importantly in $P(E)$ theory the second Hamiltonian term (Josephson tunneling) is treated as a perturbation, to compute forward $\vec{\Gamma}(V)$ and backward $\overleftarrow{\Gamma}(V)$ tunneling rates using Fermi's golden rule. The tunneling rates obey the rule $\overleftarrow{\Gamma}(V) = \vec{\Gamma}(-V)$ and are related to the $P(E)$ function according to the relation

$$\vec{\Gamma}(V) = \frac{\pi E_{\mathrm{J}}^2}{2\hbar} P(2eV) \tag{2.17}$$

Once the tunneling rates are known the $I - V$ characteristics of the junction read

$$\begin{aligned} I(V) &= 2e\left[\vec{\Gamma}(V) - \overleftarrow{\Gamma}(V)\right] \\ &= \frac{\pi e E_{\mathrm{J}}^2}{\hbar}\left[P(2eV) - P(-2eV)\right] \end{aligned} \tag{2.18}$$

From the relation above we see that the $I - V$ characteristics are directly related to the $P(E)$ function hence it is essential to understand its physical meaning.

The $P(E)$ function gives the probability for Cooper pairs to exchange energy E with the environment and tunnel inelastically across the junction by emitting a photon of energy $h\nu = 2eV$

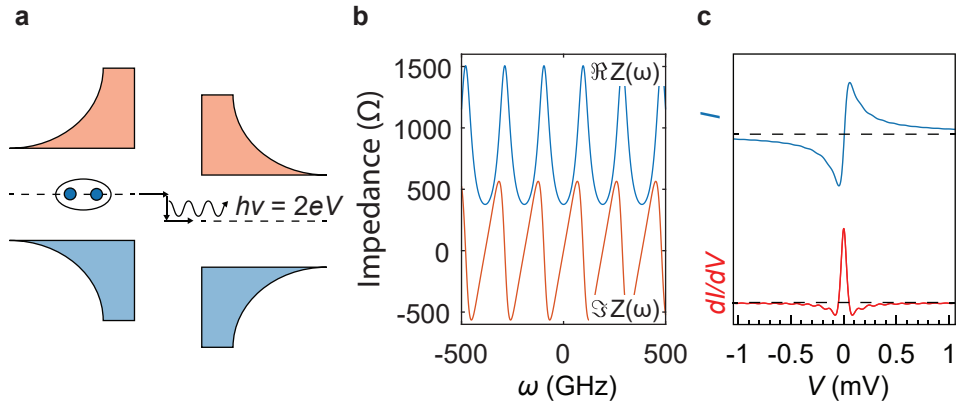

Figure 2.6: **The $P(E)$ theory.** **a** Density of states (as a function of energy and space) diagram of sequential inelastic Cooper pair tunnelling. Empty (occupied) states in the two superconducting banks are denoted by orange (blue). A Cooper pair tunnels between the two electrodes and emits a photon of energy $2eV$. **b** Real and imaginary part of the environmental impedance as calculated from equation 2.30 for $w_0 = 96.7$ GHz and $\alpha = 0.5$. **c** I–V and dI/dV curves, calculated using $P(E)$ theory for a $Z(\omega)$ corresponding to the tip-induced antenna mode in **b** of energy $h\nu = 200$ μeV and $E_T > E_C$. The I–V and dI/dV curves correspond to a voltage of V inside the gap.

This is illustrated in Fig. 2.6a. The $P(E)$ function is calculated using the following integral [26, 27, 29]

$$P(E) = (2\pi\hbar)^{-1} \int_{-\infty}^{+\infty} dt \exp\left(J(t) + iEt/\hbar\right), \tag{2.19}$$

which is the Fourier transform of the phase–phase correlation function $J(t)$

$$J(t) = \langle \Delta\phi(t)\Delta\phi(0) \rangle . \tag{2.20}$$

Here, the brackets $\langle ... \rangle$ denote the quantum mechanical average. For a given electromagnetic environment impedance $Z(\omega)$ at a junction temperature of $\beta = (k_B T)^{-1}$ the phase-phase correlator reads

$$J(t) = \int_{-\infty}^{+\infty} \frac{d\omega}{\omega} \frac{\Re Z_t(\omega)}{R_Q} \frac{\exp(-i\omega t) - 1}{1 - \exp(-\beta\hbar\omega)}. \tag{2.21}$$

We note that R_Q is the conductance quantum and Z_t the total impedance of the circuit (see Fig. 2.3) given by

$$Z_t(\omega) = \frac{1}{i\omega C_J + Z^{-1}(\omega)} \tag{2.22}$$

Calcuating the $P(E)$ function from the previous equations is a difficult task. For this reason Inglold et al [30] developed a self-consistent method for the calculation of the $P(E)$ function. It involves the following convolution integral:

$$P(E) = \mathcal{I}(E) + \int_{-\infty}^{+\infty} d\omega \mathcal{K}(E, \omega) P(E - \hbar\omega) \tag{2.23}$$

together with the normalization condition since $P(E)$ is a probability function

$$\int_{-\infty}^{\infty} P(E)dE = 1 \tag{2.24}$$

The inhomogeneity function $\mathcal{J}(E)$ reads:

$$\begin{aligned} \mathcal{J}(E) &= \frac{1}{\pi\hbar}\frac{\mathcal{D}}{\mathcal{D}^2 + E^2/\hbar^2} \\ \mathcal{D} &= \frac{\pi k_{\mathrm{B}} T}{h}\frac{\Re Z_{\mathrm{t}}(0)}{R_{\mathrm{Q}}} \end{aligned} \tag{2.25}$$

whereas the $\mathcal{K}(E,\omega)$ function (also called the integral kernel):

$$\mathcal{K}(E,\omega) = \frac{E/\hbar}{\mathcal{D}^2 + E^2/\hbar^2}k(\omega) + \frac{D}{D^2 + E^2/\hbar^2}k'(\omega) \tag{2.26}$$

with

$$k(\omega) = \frac{1}{1-\exp(-\beta\hbar\omega)}\frac{\Re Z_{\mathrm{t}}(\omega)}{R_{\mathrm{Q}}} - \frac{1}{\beta\hbar\omega}\frac{\Re Z_{\mathrm{t}}(0)}{R_{\mathrm{Q}}} \tag{2.27}$$

and

$$k'(\omega) = \frac{1}{1-\exp(-\beta\hbar\omega)}\frac{\Im Z_{\mathrm{t}}(\omega)}{R_{\mathrm{Q}}} - \frac{2}{\beta\hbar}\sum_{n=1}^{+\infty}\frac{\nu_n}{\nu_n^2 + \omega^2}\frac{Z_{\mathrm{t}}(-i\nu_n)}{R_{\mathrm{Q}}} \tag{2.28}$$

In the last relation of $\kappa(\omega)$ above, the Matsubara frequencies are denoted as $\nu_n = 2\pi n k_{\mathrm{B}} T$.

The methodology described above provides a simple and powerful method for calculating the $I-V$ characteristics of a Josephson junction subject to quantum phase fluctuations embedded in an arbitrary electromagnetic environment. As an example, in the following we will calculate the tunneling characteristics for a Josephson STM junction using the $P(E)$ formalism.

Antenna mode

In a JSTM junction the tip-probe acts as an antenna with well-defined equidistant resonant frequencies ω_n that are given by the formula [31]

$$\omega_p = (2p+1)\frac{c}{4l_t}, \quad p = 0, 1, 2... \tag{2.29}$$

where c is the speed of light and l_t is the tip length. A tip that is 3 mm long has resonant frequencies that are multiples of 25 GHz. This translates into voltage multiples of 50 μV. Given the lowest eigen frequency ω_0, the electromagnetic environment due to the antenna modes of the tip becomes [32]

$$Z(\omega) = Z(0)\frac{1 + \frac{i}{\alpha}\tan\left(\frac{\pi}{2}\frac{\omega}{\omega_0}\right)}{1 + i\alpha\tan\left(\frac{\pi}{2}\frac{\omega}{\omega_0}\right)}. \tag{2.30}$$

$Z(0)$ is the vacuum impedance, equal to 376.73 Ω and α a damping factor. Figure 2.6b shows the real and the imaginary part of the impedance for the antenna mode environment with $\alpha = 0.5$ and $\omega_0 = 96.7$ GHz. The corresponding $I-V$ and dI/dV characteristics are shown in Fig. 2.6c, as calculated using $P(E)$ theory. We see that both curves resemble the IZ model predictions. However, here one also observes small oscillations associated to the antenna mode resonances.

As a final note we want to emphasize that similar to the RCSJ and IZ model, the superconducting order parameter can be extracted by inspection or fitting of the tunneling characteristics using $P(E)$ theory. In more detail, the relation in 2.18 contains the Josephson energy as scaling factor. In turn the Josephson energy is proportional to the critical supercurrent which is a measure of the order parameter as we saw earlier.

2.2.5. Experimental procedures

In the previous sections we focused on the basic theoretical principles of JSTM that allow us to probe the superfluid density. Here we want to describe the main features of the JSTM experiments that we perform in subsequent chapters. Apart from performing the STM experiments at sufficiently low temperatures, we find that the main challenges in JSTM is preparing a superconducting tip and reducing unwanted signal noise.

There are two common approaches in preparing a superconducting STM tip. In the first one a tip wire made of a superconducting material is used whereas in the second the apex of a metallic tip is decorated with a superconducting cluster. In the case of using a superconducting wire as an STM tip, Nb, Pb and Al are usually the materials of choice. All of them need special treatment in order to make the tip apex sharp and remove any oxide layers. Such treatments are often time consuming and require multiple preparation steps outside the STM apparatus, that limit the yield of achieving a high quality superconducting tip. Nevertheless, examples of STM experiments using a superconducting wire as tip material can be found in Refs. [32–39]

In our case, we employ the method of attaching a superconducting cluster to the apex of a metallic tip. In this method all the preparation takes place in the ultra-high vacuum of the STM chamber and has been proven very successful in several experiments as described in Refs. [9, 40]. As a superconducting material, Pb is typically the target material for inducing superconducting correlations in the tip, but a cuprate superconductor [41] or MgB_2 [42] have also been reported in literature. Pb is a soft material with low melting point and good wetting properties on most surfaces. This favours to first indent a metallic tip on Pb and locally melt the surface. Subsequently, the tip is pulled away from the surface to obtain a Pb coated tip apex. Last but not least, Pb has a relatively high critical temperature (7.2 K) that does not limit the range of operation at milli-Kelvin temperatures.

In our experiments, we make superconducting STM tips by indenting a sharp metallic Pt–Ir tip into a clean Pb(111) surface. The indentations are repeated until the tip shows a pair-breaking gap equal to that of bulk Pb (ref. [43]). The bulk-like superconductivity of the tip is verified using tunnelling spectroscopy. The differ-

ential conductance spectrum exhibits a finite superconducting gap determined by two sharp coherent peaks. Because of the superconducting tip, these are much sharper than what one would expect from conventional thermal broadening. In the measured spectrum shown in Fig. 2.7a, all quasiparticle states of the sample are shifted by the superconducting gap of the tip, and thus the tunnelling spectrum clearly shows sharp coherent peaks at an energy equal to the sum of the two superconducting gaps, $\Delta_{\mathrm{CP,t}} + \Delta_{\mathrm{CP,s}} = 2.6$ meV. We fit the spectrum with the formula

$$\left(\frac{dI}{dV}\right) = \frac{G_{\mathrm{N}}}{e}\int\left\{\frac{\partial D_{\mathrm{t}}(\epsilon+eV)}{\partial V}\left[f(\epsilon)-f(\epsilon+eV)\right] - D_{\mathrm{t}}(\epsilon+eV)\frac{\partial f(\epsilon+eV)}{\partial V}\right\}D_{\mathrm{t}}(\epsilon)d\epsilon, \tag{2.31}$$

where G_{N} is the normal-state conductance, ϵ is the integration variable for energy and $f(\epsilon)$ is the Fermi–Dirac distribution at temperature T. For the density of states of the tip and sample, $D_{\mathrm{t(s)}}$, we use a modified Dynes formula [44]

$$D_{\mathrm{t(s)}} = \mathrm{Re}\left[\mathrm{sgn}(\epsilon)\frac{\epsilon}{\sqrt{\epsilon^2 + 2i\gamma\epsilon - \Delta^2_{\mathrm{CP,t(s)}}}}\right]. \tag{2.32}$$

where γ represents a phenomenological broadening term. We find good agreement between the measured data and the model for $\Delta_{\mathrm{CP,s}} = \Delta_{\mathrm{CP,t}} = 1.3$ meV, $\gamma = 45$ μeV and $T = 2.2$ K. Here, the effective temperature of 2.2 K is estimated by fitting the spectra acquired with a normal Pt–Ir tip on a Pb(111) superconducting surface (Fig. 2.7b). The parameters Δ_{CP} and γ are also free fitting parameters.

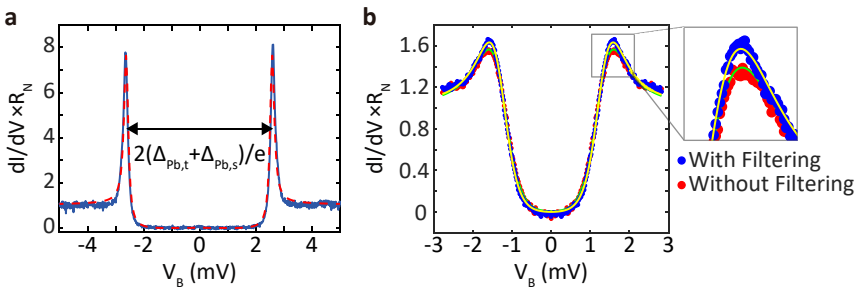

Figure 2.7: **Tunnelling spectra of Pt–Ir/Pb and Pb/Pb junctions.** **a** Normalized conductance spectrum (blue curve) of a Pb/Pb junction, acquired with a junction resistance of 5 MΩ ($V_{\mathrm{set}} = +5$ mV, $I_{\mathrm{set}} = 1.0$ nA). The fit (red dashed curve) is consistent with the quasiparticle spectrum of a symmetric Josephson junction with a pair-breaking gap of 1.3 meV at 2.2 K. **b** Differential tunnelling spectra of a Pt–Ir/Pb junction with (blue dots) and without (red dots) electronic filtering using home-built lumped-element low-pass filters in series with commercial 1.9-MHz low-pass filters and grounding for all non-essential lines ($V_{\mathrm{set}} = +5$ mV, $I_{\mathrm{set}} = 0.10$ nA). We use a modified Dynes formula to fit our spectra, and the results give effective temperatures of 2.38 K (green line) and 2.20 K (yellow line). The other parameters are the same in both cases ($\Delta_{\mathrm{CP}} = 1.30$ meV and $\gamma = 50$ μeV).

Last but not least, we want to stress out the importance of filtering the signal lines in order to reduce unwanted noise and enhance the tunneling signal. The

benefit of electronic filtering was already suggested in early JSTM experiments by Rodrigo et al. [45]. We followed a similar approach by using ~ 2 MHz commercial low-pass filters in series with home-built low pass filters. In addition, all lines that are not used for the STM or conductance measurement were grounded. In practice, by employing the filters that we describe before results, in conductance spectra where the extracted electron temperature is lower. An example is shown in Fig. 2.7b.

2.3. Noise scanning tunneling microscopy

Noise scanning tunneling microscopy is a technique that aims at measuring the shot noise in an STM junction. Shot noise measurements using conventional STM circuitry are prohibited due to the fact that the GΩ tunneling resistance combined with the cabling capacitance form a low-pass kHz filter. As a result, detection of the tunneling current in conventional STM is only possible in a bandwidth range between DC and a few kHz. Importantly, in this frequency range unwanted noise sources (mechanical and $1/f$ flicker noise) are present which influence the tunneling signal. This suggests that shot noise measurements should be performed in a higher frequency regime. In the high-frequency range, thermal and shot noise are the dominant current fluctuations of the tunneling signal.

Thermal and shot noise are frequency independent (white noise behaviour) and provide information about the system under consideration. Thermal or Johnson-Nyquist noise is a result of thermal agitation events in a system. Such events cause dynamic fluctuations of the number state occupancy. The power spectral density of the thermal noise in a conductor with a finite resistance R' is given by $S_{\mathrm{th}} = 4k_{\mathrm{B}}T/R'$, where k_{B} is Boltzmann's constant and T is the temperature. Since thermal noise in a conductor is proportional to the temperature, it can be lowered by reducing the temperature. Thermal noise effects can be discerned from shot noise at zero tunneling current, where the latter vanishes.

Shot noise is a consequence of electronic charge quantization. Importantly, the latter has no effect on the mean (time-averaged) value of a current or conductance measurement. On the other hand, by performing shot noise measurements we can determine the charge and the statistics of the carriers that contribute to transport. Shot noise is frequency independent and in the case of uncorrelated electron (charge e) transport exhibiting average current I it reads

$$S_{\mathrm{P}} = 2eI. \tag{2.33}$$

The above formula represents uncorrelated transport governed by Poissonian processes [46].

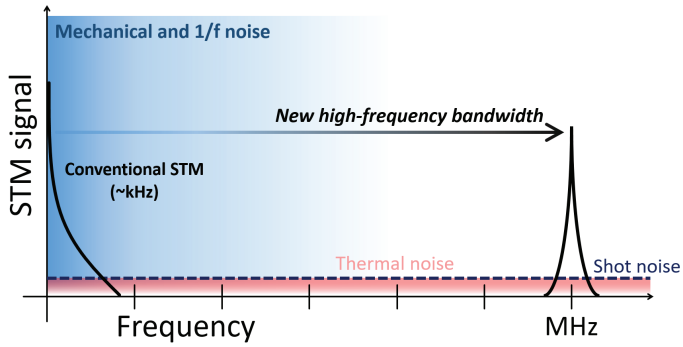

Figure 2.8: **Noise sources in STM.** Schematic plot of the noise sources that are present in an STM experiment as a function of frequency. Mechanical and $1/f$ unwanted noise dominate in the low-frequency regime where conventional STM circuitry operates. In the high-frequency regime thermal and shot noise are the most dominant, exhibiting no frequency dependence. Thus, in a tunneling shot noise experiment it is important to shift the STM bandwidth to higher frequencies.

Fig. 2.8 depicts a schematic of the various noise sources in STM as a function of frequency. It becomes apparent that measuring the shot noise is an STM junction requires operation at high frequencies. Next, we review how the bandwidth in STM can be extended to MHz frequencies making it possible to measure the shot noise [47].

2.3.1. STM noise circuitry

NSTM in our experiments is achieved by employing a resonance circuit based amplifier in a commercial STM setup. It includes a bias-tee based on a resonator. Fig. 2.9 shows a simplified circuit diagram. The STM junction under bias V is described by a resistance R_{J} and capacitance C_{J}. The tunneling current signal I_{J} signal is separated into high- and low-frequency components with the use of the resonator based bias-tee that follows (blue dashed rectangle). The low-frequency component is essential for performing conventional STM imaging and spectroscopy and is subsequently converted to a voltage via a room temperature amplifier.

The high-frequency component subsequently passes through a parallel RLC tank. The tank circuit converts the current to voltage at the resonance frequency $f_0 = \left(2\pi\sqrt{LC}\right)^{-1}$ over the tank (orange dashed rectangle) which is detected by the gate of a high electron mobility transistor (HEMT) [48]. The HEMT operates at cryogenic temperatures and exhibits very low input referred voltage and current noise. Voltage fluctuations at the gate of HEMT are converted into current fluctuations which are measured over a 50 Ω resistor. Next a 50 Ω coaxial line connects the amplifier circuit to a 40 dB current amplifier at room temperature. Finally, the signal line is terminated by the 50 Ω input impedance of a spectrum analyser.

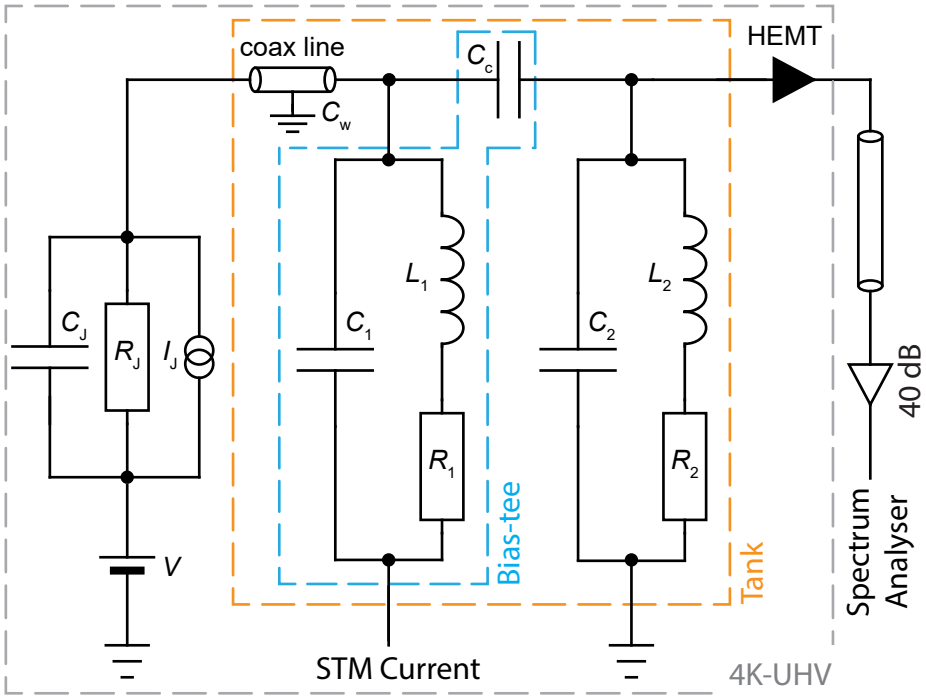

Figure 2.9: **Circuit schematic for NSTM.** Circuit for NSTM consisting of a bias-tee (blue dashed rectangle) and a tank circuit (orange dashed rectangle). The junction is under bias voltage V characterised by a resistance R_J and capacitance C_J. The tunneling signal I_J is decomposed to its low- and high-frequency parts using a resonator-based bias-tee and a double-tank circuit. A high electron mobility transistor at cryogenic temperatures and ultra-high vacuum (4K-UHV) is employed for amplifying the high-frequency signal. The high frequency signal is subsequently amplified (40 dB amplifier) and measured with a spectrum analyser.

Circuit elements

The circuit that we analysed previously was implemented on a special circuit board (suitable for ultra-high vacuum applications) in combination with homemade and commercial elements [47]. Here we highlight some important features:

- The two inductors in the tank circuit are home-made using superconducting Nb wire. This way the quality factor of the resonator is enhanced, increasing current-to-voltage amplification at resonance.
- The tank circuit is covered with a Nb shield to minimize Eddy current damping. This way the quality factor of the resonator is as high as possible.
- To ensure linear gate voltage to current conversion, the HEMT operates in saturation.

To summarize up to now, we have seen the basic principles of NSTM and the importance of measuring the shot noise at high-frequencies. In addition, we analysed

the noise circuit design that allows to measure shot noise in an STM junction. Next, we proceed by considering how the shot noise can be quantitatively extracted from NSTM measurements.

2.3.2. Extracting the shot noise

The measurement of the shot noise via the scheme that we described previously boils down to recording the high-frequency oscillations of the tunneling signal I_{J} in the spectrum analyser (see Fig. 2.9). The central idea behind the extraction of the shot noise from such a measurement is to fit the measured power spectral density with an appropriate model. Therefore, this model should include, among others, the shot noise as a fitting parameter allowing this way its quantitative determination. We will follow two different approaches here. The first model is based on phenomenology and takes into account the effect of the electromagnetic environment of the tunnel junction in order to describe the total current fluctuations. The second approach is simpler and is what we will use in practice in Chapters 5 and 6. In this approach we employ a circuit diagram fit for the measured power spectral density and extract the shot noise of the junction.

Phenomenological treatment

In this model, circuit theory is employed in order to derive the current noise spectrum of a tunneling junction embedded in an environment characterised by its impedance. The model is based on the work of Frey and Grabert [49] which combines phenomenological arguments with circuit theory. Importantly, it is shown that is accurately reproduces earlier results based on a Hamiltonian model approach [50].

In a nutshell, using this model we will calculate the power spectral density measured at the spectrum analyser of our setup. In order to proceed with the calculations it is useful to first define the frequency dependent (ω) admittances $Y_{\mathrm{L,R}}$ at the left (L) and right (R) of the coax line shown in Fig. 2.9

$$\begin{aligned} Y_{\mathrm{L}} &= \frac{1}{Z_{\mathrm{L}}} = -i\omega C_{\mathrm{J}} \\ Y_{\mathrm{R}} &= \frac{1}{Z_{\mathrm{R}}} = \frac{1}{Z_1 + i/(\omega C_{\mathrm{w}})} + \frac{1}{Z_2 + i/(\omega C_{\mathrm{c}})}. \end{aligned} \tag{2.34}$$

Here, $Y_{1,2}$ are the admittances of the two resonators in the tank circuit. They read

$$Y_j = \frac{1}{Z_j} = \frac{1}{R_j - i\omega L_j} - i\omega C_j = \frac{1 - \omega^2 C_j L_j - i\omega C_j R_j}{R_j - I\omega L_j}. \tag{2.35}$$

After some work which we do not intend to show here, the measured voltage $V_{\mathrm{m}}(\omega)$ is found to be

$$-\frac{V_{\mathrm{m}}}{N_0} = \frac{\mathcal{W} Z_{\mathrm{L}} Z_{\mathrm{R}}}{Z_{\mathrm{L}} + Z_{\mathrm{R}}} i_{\mathrm{T}} + \frac{i}{\omega C_2} i_2 + \frac{\mathcal{W} Z_{\mathrm{R}} \left[Z_{\mathrm{L}} \cos(\omega l/v) - i Z_0 \sin(\omega l/v) \right]}{Z_{\mathrm{L}} + Z_{\mathrm{R}}} \sum_{p=1,2} A_p i_p. \tag{2.36}$$

Here

$$A_p = \frac{Z_p}{Z_p + i/(\omega C_p')}, \tag{2.37}$$

where we have defined $C_1' = C_{\mathrm{w}}$, $C_2' = C_{\mathrm{c}}$ and N_0 is given by

$$N_0 = \frac{Z_2}{Z_2 + i/(\omega C_{\mathrm{c}})}. \tag{2.38}$$

We see in 2.36 that the measured voltage is a linear combination of the shot noise $i_{\mathrm{T}}(\omega)$ of the tunnel junction and the noise currents $i_1(\omega)$ and $i_2(\omega)$ of the resistors in the tank resonators. Moreover, $\mathcal{W}$ is the characteristic transmission through the coax line and is given by

$$\mathcal{W} = \frac{Z_0(Z_{\mathrm{L}} + Z_{\mathrm{R}})}{Z_0(Z_{\mathrm{L}} + Z_{\mathrm{R}})\cos(\omega l/v) - i(Z_0^2 + Z_{\mathrm{L}}Z_{\mathrm{R}})\sin(\omega l/v)}. \tag{2.39}$$

In the formula above, the coaxial cable is of length l with a characteristic impedance Z_0. In addition, v represents the phase velocity.

The noise spectrum of the measured voltage V_{m} is the average (denoted as $\langle\ldots\rangle$) of the fluctuation correlator. It reads

$$S_V(\omega) = \langle \delta V_{\mathrm{m}}(\omega)\delta V_{\mathrm{m}}(-\omega)\rangle, \tag{2.40}$$

where the fluctuations $\delta V_{\mathrm{m}}(\omega)$ are defined as the following Fourier transform

$$\delta V_{\mathrm{m}}(\omega) = \Im\left[V_{\mathrm{m}}(t) - \langle V_{\mathrm{m}}(t)\rangle\right] \tag{2.41}$$

Therefore, inserting 2.36 in 2.40 allows us to calculate the noise spectrum that we measure experimentally in NSTM. By close examination we observe that the noise spectrum $S_V(\omega)$ will be a linear combination of various correlations [49, 50]. The first one is the noise form the junction

$$\left\langle i_{\mathrm{T}}(\omega) i_{\mathrm{T}}(\omega')\right\rangle = S(\omega) 2\pi\delta(\omega + \omega'), \tag{2.42}$$

with the shot noise spectrum given by

$$S(\omega) = \frac{eI(V - \hbar\omega/e)}{\exp\left[\beta(eV - \hbar\omega)\right] - 1} + \frac{eI(V + \hbar\omega/e)}{1 - \exp\left[\beta(eV + \hbar\omega)\right]}. \tag{2.43}$$

Here, $I(V)$ is the current-voltage characteristic of the junction and $\beta = 1/(k_{\mathrm{B}}T)$. The second correlation concerns the thermal noise; the Johnson-Nyquist noise of resistors

$$\left\langle i_p(\omega) i_{p'}(\omega')\right\rangle = \frac{2\hbar\omega}{1 - \exp(-\beta\hbar\omega)} \frac{\delta_{pp'}}{R_p} 2\pi\delta(\omega + \omega'). \tag{2.44}$$

Last but not least, the cross-correlation noise between the shot noise contribution and the thermal noise term. It is expressed by the following relation

$$\left\langle i_{\mathrm{T}}(\omega) i_p(\omega')\right\rangle = Y_{\mathrm{J}}(\omega, V) Z_{p\mathrm{J}}(\omega) \frac{1}{R_p} 2\pi\delta(\omega + \omega'). \tag{2.45}$$

The admittance Y_{J} of the junction reads

$$Y_{\mathrm{J}}(\omega,V)=\frac{e}{2\hbar\omega}\Big[I(V+\hbar\omega/e)-I(V-\hbar\omega/e)-iI_{\mathrm{KK}}(V+\hbar\omega/e) \\ -iI_{\mathrm{KK}}(V-\hbar\omega/e)+2iI_{\mathrm{KK}}(V)\Big], \tag{2.46}$$

where $I_{\mathrm{KK}}(V)$ is the Kramers-Kronig transform of the $I(V)$ characteristics. It reads

$$I_{\mathrm{KK}}=P\int_{-\infty}^{+\infty}\frac{dU}{\pi}\frac{I(U)-G_{\mathrm{T}}U}{U-V}. \tag{2.47}$$

Here P denotes the principal value and G_{T} the conductance of the junction. In addtion, the impedance $Z_{p\mathrm{J}}$ in 2.45 characterizes the coupling strength of the noise i_p to the junction

$$Z_{p\mathrm{J}}=-\frac{\mathcal{W}Z_{\mathrm{L}}Z_{\mathrm{R}}}{Z_{\mathrm{L}}+Z_{\mathrm{R}}}\frac{Z_p}{Z_p+i/(\omega C_p')}. \tag{2.48}$$

In Figure 2.10a we plot the frequency-dependent total impedance of the noise circuit and voltage noise by using the circuit theory model that we described before. The total impedance in this framework reads

$$Z_{\mathrm{t}}(\omega)=\frac{Z_{\mathrm{L}}Z_0}{Z_{\mathrm{L}}+Z_0}\left[1+\frac{\mathcal{W}Z_{\mathrm{L}}(Z_{\mathrm{R}}-Z_0)\exp(i\omega l/v)}{Z_0(Z_{\mathrm{L}}+Z_{\mathrm{R}})}\right], \tag{2.49}$$

and as we can see from the plot, it exhibits a pronounced resonance peak at MHz frequencies. In more detail, the resonance of the circuit is formed by the self-resonance of the superconducting Nb inductors in combination with the coaxial cable. Choosing $L_1=L_2=66\ \mu$H and $C_{\mathrm{w}}=30$ pF yields a resonance frequency at ~ 3 MHz. The circuit element values that we used above were chose specifically for extending the STM bandwidth as we explained in the previous section. The same values were chosen for the experimental realization of the NSTM circuit that is employed in Chapters 5 and 6. As far as the noise spectrum is concerned (2.10b) it also exhibits a resonant behaviour at MHz frequencies. At this point, we do not intend to elaborate on the extraction of the shot noise associated in such a calculation. Even though it is possible to do it using the formulas that we presented previously, it becomes cumbersome thus impractical for an experimental analysis. We therefore proceed to the description of the second model that is simpler and is used in practice.

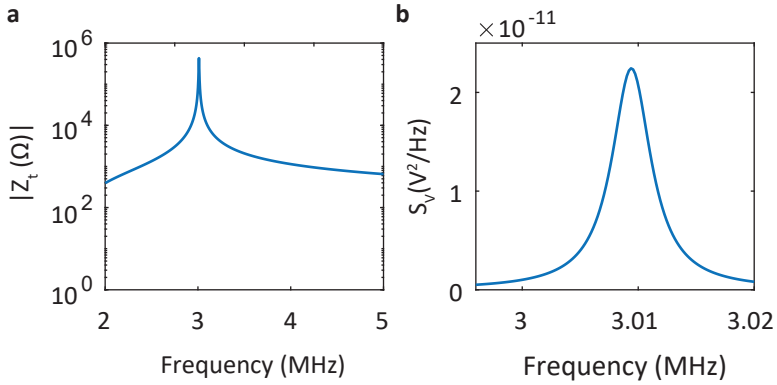

Figure 2.10: **Circuit theory model simulations. a** Absolute value of the total impedance of the noise circuit calculated using the circuit theory model. Two resonance peaks at MHz frequencies are observed. **b** Calculated voltage noise as a function of frequency using the circuit theory model described in the text. For the calculation we assumed an Ohmic junction with $R_J = 1$ GΩ, at $T = 3.2$ K. The junction is biased with $V = 5$ mV. For both panels we used the same parameters: $C_J = 1$ fF, $C_1 = C_2 = 15$ pF, $L_1 = L_2 = 66$ μH, $R_1 = R_2 = 1.7$ Ω, $C_c = 100$ pF and $C_w = 30$ pF. For the coax line: $l = 30$ cm and $Z_0 = 50$ Ω.

Circuit diagram fit

In this section we shall see how we extract the shot noise in a NSTM experiment using a circuit diagram fit. As already stated, the procedure that we will describe here is employed for all the shot noise measurements presented in this thesis.

First let us recall that in a NSTM experiment the measured quantity is the voltage noise over the 50 Ω input resistance of our spectrum analyser (see Fig. 2.9). It depends on the bias voltage V and in the frequency domain is given by the expression [46]

$$S_V^m(\omega, V) = G^2 |Z_{\mathrm{res}}^2| S_I. \tag{2.50}$$

Here G is the total gain of the amplification chain. Z_{res} is the impedance of the resonating circuit and S_I is the total current noise in the circuit. From this expression we clearly see that Z_{res} influences the measured spectrum, thus our first step is to fit the measured spectrum in order to mitigate the effect of a possibly non-linear differential conductance $dI(V)/dV$ on the effective resonator impedance. This is particularly important when measuring the voltage noise spectrum in a superconducting material; the dI/dV in a superconductor is not constant for voltages inside the superconducting gap Δ. To illustrate this in Fig. 2.11 we present voltage noise measurements in Pb/Pb JSTM junction (similar to the one shown in Fig. 2.7a) for different bias voltages exhibiting strong dI/dV variations. The clear change of the measured power spectral density for varying bias voltage is due to the simultaneously changing impedance of the resonator and the amplitude of the current noise as a function of bias.

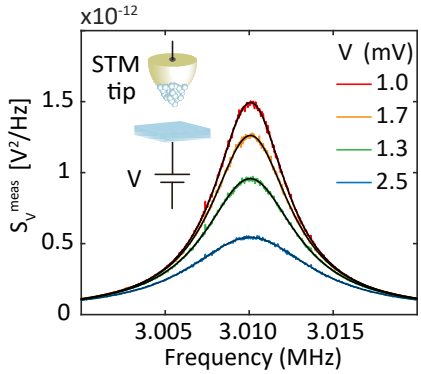

Figure 2.11: **Voltage noise measurement in a Pb/Pb STM junction.** Power spectral density of the resonator circuit, in a small bandwidth around the resonance frequency for a Pb/Pb STM junction at 2.2 K. The different spectra represent various applied bias to the Josephson junction. Measured data is plotted by the colored lines, the black curves correspond to a circuit diagram fit. The inset shows a schematic of the STM junction.

From the fitted voltage noise spectrum we extract the current noise S_I which consists of three terms:

$$S_I(I) = 2q^* I \coth\left(\frac{q^* V}{2k_{\mathrm{B}}T}\right) + \frac{4k_{\mathrm{B}}T}{|Z_{\mathrm{res}}|} + S_{\mathrm{amp}}, \tag{2.51}$$

where q^* is the effective carrier charge and S_{amp} the input noise of the amplifier. Importantly, the first term represents the shot noise spectrum that we want to extract. One can show that it is obtained from 2.43 for $eV \gg h\omega$ and $k_{\mathrm{B}}T \gg h\omega$ which holds in the MHz regime. The second term is the thermal noise of the LC tank resonator.

To numerically extract the shot noise and the effective charge q^* from the measured noise the following method is followed. For retrieving the desired shot noise contribution we subtract the out-of-tunneling, zero-current noise $S_I(0)$ from the current noise measured in tunneling $S_I(I)$. The zero-current noise corresponds to the contributions from the thermal noise of the tank and amplifier noise. Hence after subtraction we are left with

$$S_I(I) - S_I(0) = 2q^* I \coth\left(\frac{q^* V}{2k_{\mathrm{B}}T}\right). \tag{2.52}$$

Finally, we extract the effective charge $q^*(V,T)$ for each V and T numerically by finding the least square solution of

$$\left(S_I^m - S_I\right)^2 = 0, \tag{2.53}$$

with respect to $q*$. Note, that we have introduced the superscript m in order to denote the measured current spectrum.

References

[1] G. Binnig and H. Rohrer, *Scanning tunneling microscopy,* Surf. Sci. **126**, 236 (1983).

[2] J. E. Hoffman, *Spectroscopic scanning tunneling microscopy insights into Fe-based superconductors,* Rep. Prog. Phys. **74**, 124513 (2011).

[3] H. G. Le Duc, W. J. Kaiser, and J. A. Stern, *Energy-gap spectroscopy of superconductors using a tunneling microscope,* Appl. Phys. Lett. **50**, 1921 (1987).

[4] J. R. Kirtley, S. I. Raider, R. M. Feenstra, and A. P. Fein, *Spatial variation of the observed energy gap in granular superconducting NbN films,* Appl. Phys. Lett. **50**, 1607 (1987).

[5] A. L. de Lozanne, S. A. Elrod, and C. F. Quate, *Spatial Variations in the Superconductivity of Nb_3Sn Measured by Low-Temperature Tunneling Microscopy,* Phys. Rev. Lett. **54**, 2433 (1985).

[6] H. F. Hess, R. B. Robinson, and J. V. Waszczak, *Vortex-core structure observed with a scanning tunneling microscope,* Phys. Rev. Lett. **64**, 2711 (1990).

[7] H. F. Hess, R. B. Robinson, R. C. Dynes, J. M. Valles, and J. V. Waszczak, *Scanning-Tunneling-Microscope Observation of the Abrikosov Flux Lattice and the Density of States near and inside a Fluxoid,* Phys. Rev. Lett. **62**, 214 (1989).

[8] A. Yazdani, B. A. Jones, C. P. Lutz, M. F. Crommie, and D. M. Eigler, *Probing the Local Effects of Magnetic Impurities on Superconductivity,* Science **275**, 1767 (1997).

[9] B. W. Heinrich, J. I. Pascual, and K. J. Franke, *Single magnetic adsorbates on s-wave superconductors,* Prog. Surf. Sci. **93**, 1 (2018).

[10] A. K. Gupta, L. Crétinon, N. Moussy, B. Pannetier, and H. Courtois, *Anomalous density of states in a metallic film in proximity with a superconductor,* Phys. Rev. B **69**, 104514 (2004).

[11] M. Wolz, C. Debuschewitz, W. Belzig, and E. Scheer, *Evidence for attractive pair interaction in diffusive gold films deduced from studies of the superconducting proximity effect with aluminum,* Phys. Rev. B **84**, 104516 (2011).

[12] M. Ruby, B. W. Heinrich, J. I. Pascual, and K. J. Franke, *Experimental Demonstration of a Two-Band Superconducting State for Lead Using Scanning Tunneling Spectroscopy,* Phys. Rev. Lett. **114**, 157001 (2015).

[13] M. Müller, N. Néel, S. Crampin, and J. Kröger, *Lateral Electron Confinement with Open Boundaries: Quantum Well States above Nanocavities at Pb(111),* Phys. Rev. Lett. **117**, 136803 (2016).

[14] O. Fischer, M. Kugler, I. Maggio-Aprile, C. Berthod, and C. Renner, *Scanning tunneling spectroscopy of high-temperature superconductors,* Rev. Mod. Phys. **79**, 353 (2007).

[15] T. Hanaguri, Y. Kohsaka, M. Ono, M. Maltseva, P. Coleman, I. Yamada, M. Azuma, M. Takano, K. Ohishi, and H. Takagi, *Coherence Factors in a High-T_c Cuprate Probed by Quasi-Particle Scattering Off Vortices,* Science **323**, 923 (2009).

[16] B. B. Zhou, S. Misra, E. H. da Silva Neto, P. Aynajian, R. E. Baumbach, J. Thompson, E. D. Bauer, and A. Yazdani, *Visualizing nodal heavy fermion superconductivity in $CeCoIn_5$,* Nat. Phys. **9**, 474 (2013).

[17] J. Šmakov, I. Martin, and A. V. Balatsky, *Josephson scanning tunneling microscopy,* Phys. Rev. B **64**, 212506 (2001).

[18] B. Josephson, *Possible new effect in superconducting tunneling,* Phys. Lett. **1**, 251 (1962).

[19] R. Fagaly, *Superconducting quantum interference device instruments and applications,* Rev. Sci. Instrum. **77**, 101101 (2006).

[20] F. Arute, K. Arya, R. Babbush, D. Bacon, J. C. Bardin, R. Barends, R. Biswas, S. Boixo, F. G. Brandao, D. A. Buell, *et al.*, *Quantum supremacy using a programmable superconducting processor,* Nature **574**, 505 (2019).

[21] M. Tinkham, *Introduction to Superconductivity*, Dover Books on Physics Series (Dover Publications, 2004).

[22] V. Ambegaokar and A. Baratoff, *Tunneling between superconductors,* Phys. Rev. Lett. **10**, 486 (1963).

[23] W. C. Stewart, *CURRENT-VOLTAGE CHARACTERISTICS OF JOSEPHSON JUNCTIONS,* Appl. Phys. Lett. **12**, 277 (1968).

[24] D. E. McCumber, *Effect of ac Impedance on dc Voltage-Current Characteristics of Superconductor Weak-Link Junctions,* J. Appl. Phys. **39**, 3113 (1968).

[25] Y. Ivanchenko and L. Zil'Berman, *The Josephson effect in small tunnel contacts,* Sov. Phys. JETP **28** (1969).

[26] Y. V. Nazarov and G.-L. Ingold, *NATO ASI Series B*, Vol. 294 (Plenum Press, New York, 1992, 1992) pp. 21–107.

[27] D. Averin, Y. Nazarov, and A. Odintsov, *Incoherent tunneling of the cooper pairs and magnetic flux quanta in ultrasmall Josephson junctions,* Physica B **165-166**, 945 (1990).

[28] A. Caldeira and A. Leggett, *Quantum tunnelling in a dissipative system,* Ann. Phys.-NEW YORK **149**, 374 (1983).

[29] G.-L. Ingold, H. Grabert, and U. Eberhardt, *Cooper-pair current through ultrasmall Josephson junctions,* Phys. Rev. B **50**, 395 (1994).

[30] G.-L. Ingold and H. Grabert, *Finite-Temperature Current-Voltage Characteristics of Ultrasmall Tunnel Junctions,* Europhys. Lett. **14**, 371 (1991).

[31] B. Jäck, M. Eltschka, M. Assig, A. Hardock, M. Etzkorn, C. R. Ast, and K. Kern, *A nanoscale gigahertz source realized with Josephson scanning tunneling microscopy,* Appl. Phys. Lett. **106**, 013109 (2015).

[32] C. R. Ast, B. Jäck, J. Senkpiel, M. Eltschka, M. Etzkorn, J. Ankerhold, and K. Kern, *Sensing the quantum limit in scanning tunnelling spectroscopy,* Nat. Commun. **7** (2016).

[33] I. Guillamon, H. Suderow, S. Vieira, and P. Rodiere, *Scanning tunneling spectroscopy with superconducting tips of Al,* Physica C **468**, 537 (2008), proceedings of the Fifth International Conference on Vortex Matter in Nanostructured Superconductors.

[34] J. G. Rodrigo, H. Suderow, and S. Vieira, *On the use of STM superconducting tips at very low temperatures,* Eur. Phys. J. B **40**, 483 (2004).

[35] O. Naaman, W. Teizer, and R. Dynes, *Fluctuation dominated Josephson tunneling with a scanning tunneling microscope,* Phys. Rev. Lett. **87**, 097004 (2001).

[36] H. Kimura, R. P. Barber, S. Ono, Y. Ando, and R. C. Dynes, *Scanning Josephson Tunneling Microscopy of Single-Crystal* $\mathrm{Bi_2Sr_2CaCu_2O_{8+\delta}}$ *with a Conventional Superconducting Tip,* Phys. Rev. Lett. **101**, 037002 (2008).

[37] *Plasma etching of superconducting Niobium tips for scanning tunneling microscopy,* J. Appl. Phys. **116**, 014308 (2014).

[38] T. Proslier, A. Kohen, Y. Noat, T. Cren, D. Roditchev, and W. Sacks, *Probing the superconducting condensate on a nanometer scale,* Europhys. Lett. **73**, 962 (2006).

[39] X. Liu, Y. X. Chong, R. Sharma, and J. C. S. Davis, *Discovery of a Cooper-Pair Density Wave State in a Transition-Metal Dichalcogenide,* (2021), arXiv:2007.15228 [cond-mat.supr-con] .

[40] K. J. Franke, G. Schulze, and J. I. Pascual, *Competition of Superconducting Phenomena and Kondo Screening at the Nanoscale,* Science **332**, 940 (2011).

[41] M. Hamidian, S. Edkins, S. H. Joo, A. Kostin, H. Eisaki, S. Uchida, M. Lawler, E.-A. Kim, A. Mackenzie, K. Fujita, *et al.*, *Detection of a Cooper-pair density wave in* $Bi_2Sr_2CaCu_2O_{8+x}$, Nature **532**, 343 (2016).

[42] N. Bergeal, Y. Noat, T. Cren, T. Proslier, V. Dubost, F. Debontridder, A. Zimmers, D. Roditchev, W. Sacks, and J. Marcus, *Mapping the superconducting condensate surrounding a vortex in superconducting V_3Si using a superconducting MgB_2 tip in a scanning tunneling microscope,* Phys. Rev. B **78**, 1 (2008).

[43] M. Ruby, B. W. Heinrich, J. I. Pascual, and K. J. Franke, *Experimental Demonstration of a Two-Band Superconducting State for Lead Using Scanning Tunneling Spectroscopy,* Phys. Rev. Lett. **114**, 157001 (2015).

[44] R. C. Dynes, V. Narayanamurti, and J. P. Garno, *Direct Measurement of Quasiparticle-Lifetime Broadening in a Strong-Coupled Superconductor,* Phys. Rev. Lett. **41**, 1509 (1978).

[45] J. Rodrigo, V. Crespo, and S. Vieira, *Josephson current at atomic scale: Tunneling and nanocontacts using a STM,* Physica C **437-438**, 270 (2006).

[46] Y. Blanter and M. Büttiker, *Shot noise in mesoscopic conductors,* Phys. Rep. **336**, 1 (2000).

[47] K. M. Bastiaans, T. Benschop, D. Chatzopoulos, D. Cho, Q. Dong, Y. Jin, and M. P. Allan, *Amplifier for scanning tunneling microscopy at MHz frequencies,* Rev. Sci. Instrum. **89**, 093709 (2018).

[48] Q. Dong, Y. X. Liang, D. Ferry, A. Cavanna, U. Gennser, L. Couraud, and Y. Jin, *Ultra-low noise high electron mobility transistors for high-impedance and low-frequency deep cryogenic readout electronics,* Appl. Phys. Lett. **105**, 013504 (2014).

[49] M. Frey and H. Grabert, *Current noise in tunnel junctions,* Fortschr. Physik **65**, 1600055 (2017).

[50] M. Frey and H. Grabert, *Effect of the electromagnetic environment on current fluctuations in driven tunnel junctions,* Phys. Rev. B **94**, 045429 (2016).